energies

MDPI

Article

A Hybrid FNN-P&O Scheme for Maximum Power Point Tracking in Photovoltaic-Fed Boost Converters

Gang Gyoo Jin [1], Uyanga Otgonbayar [1], Otgonbaatar Yura [1], Yunhyung Lee [2] and Jooyeon Lee [3,*]

[1] Department of IT, Huree College of ICT, Ulaanbaatar 16061, Mongolia; gjin30@huree.edu.mn (G.G.J.); uyanga.o@huree.edu.mn (U.O.); otgonbaatar@huree.edu.mn (O.Y.)
[2] Ocean Technology Training Team, Korea Institute of Maritime and Fisheries Technology, Busan 49111, Republic of Korea; domse54@daum.net
[3] Ocean Space Development & Energy Research Department, Korea Institute of Ocean Science and Technology, Busan 49111, Republic of Korea
* Correspondence: leejy@kiost.ac.kr; Tel.: +82-51-664-3541

Abstract

Maximum Power Point Tracking (MPPT) under non-uniform environmental conditions, particularly partial shading, presents a significant challenge due to the emergence of multiple peaks on the power-voltage curve. Gradient-based algorithms frequently get trapped in local maxima, causing substantial energy loss. To overcome these limitations, this paper presents a novel hybrid MPPT control scheme that combines a Feedforward Neural Network (FNN) with the standard Perturb and Observe (P&O) algorithm for a PV-fed DC-DC boost converter system. First, a single-diode model for a PV cell is established, and its parameters are extracted using a hybrid genetic algorithm. The three-layer feedforward neural network (FNN) is trained offline using varying irradiance, temperature inputs, and the precalculated optimal duty cycle (D_{mpp}). During operation, the trained FNN directly estimates the operating point near the Global Maximum Power Point (GMPP) via an adaptive updating mechanism. Subsequently, a small-step P&O algorithm performs localized fine-tuning to ensure steady-state accuracy and suppress steady-state power oscillations. Simulation results conducted in MATLAB/Simulink demonstrate that under standard test conditions, dynamic partial shading, and temperature variations, the proposed FNN-P&O scheme significantly outperforms conventional and adaptive P&O algorithms by reducing transient power undershoots, preventing local entrapment, and ensuring rapid, accurate GMPP convergence.

Keywords: photovoltaic; boost converter; global maximum power point; feedforward neural network; hybrid FNN-P&O MPPT algorithm

Academic Editor: Wilfried Van Sark

Received: 4 September 2026
Revised: 16 October 2026
Accepted: 19 November 2026
Published: 23 November 2026

Copyright: © 2026 by the authors. Licensee MDPI, Basel, Switzerland. This article is an open access article distributed under the terms and conditions of the Creative Commons Attribution (CC BY) license.

1. Introduction

Global environmental challenges have accelerated intensive research into renewable energy technologies, primarily centering on solar and wind power generation [1,2]. Among these solutions, photovoltaic (PV) systems offer direct conversion of solar radiation into electrical power. Despite high initial capital expenditure, global PV deployment continues to expand rapidly worldwide due to its zero emissions and vast resource potential. However, PV cells exhibit nonlinear *I-V* and *P-V* output characteristics that vary continuously with irradiance and temperature. Consequently, maximum power point

 https://doi.org/10.3390/en19235685

tracking (MPPT) control is critical to maximize energy extraction under varying environmental conditions.

High-fidelity modeling and precise parameter estimation of PV sources are essential for designing accurate MPPT controllers and evaluating power electronic interfaces. The literature offers several equivalent circuit models, ranging from basic ideal representations (3-parameter) to single-diode (5-parameter) and two-diode configurations (7-parameter) for this purpose [1–4]. The single-diode model remains the standard benchmark due to its optimal balance of mathematical precision and computational simplicity. Robust optimization techniques, such as genetic algorithms (GAs) and particle swarm optimization (PSO), enable accurate parameter estimation of these models, allowing physical module behavior to be simulated with high fidelity under diverse operational profiles [5–7].

A DC-DC converter acts as an intermediate stage to resolve the severe impedance mismatch and resulting power losses that occur when connecting a PV panel directly to a static load. By adjusting the switching duty cycle, the MPPT controller functions as a dynamic impedance matching network, aligning load impedance with the internal resistance of the PV source. Under partial shading conditions (PSCs)—caused by clouds, trees, or nearby buildings—PV strings display multiple peaks on their power curve, containing several local maxima and one global maximum. Standard local search algorithms like perturb and observe (P&O) and incremental conductance (IncCond) offer simplicity and low computational overhead [1,2,8–11]. To enhance search performance, methods for adaptively adjusting the step size of the P&O method have been investigated [12,13]. Nevertheless, since they terminate the search when $dP/dV = 0$, the gradient-based algorithms frequently get trapped at local maxima under PSCs or non-uniform irradiance.

Recently, various metaheuristic algorithms, including GAs [14–16], PSO [17–19], and whale optimization (WO) [20], have been applied to MPPT control to overcome local entrapment issues. In [21], an MPPT control strategy powered by combining WO for global exploration with the sparrow search algorithm for local exploitation has been proposed. Nagadurga et al. [22] evaluated metaheuristic optimization algorithms including PSO, cat swarm optimization, teaching–learning-based optimization, gray wolf optimization and chimp optimization to overcome local peak trapping in partially shaded PV arrays. Although metaheuristic strategies can successfully bypass local optima to locate the global maximum power point (GMPP), they introduce severe implementation challenges in real-time hardware. Population-based optimization requires evaluating multiple candidate solutions iteratively during live system operation. Evaluating bad candidates often triggers prolonged electrical transients, causes thermal or voltage stress, and imposes significant computational overhead on the microcontroller. Consequently, AI-based MPPT methods have emerged to address these critical drawbacks, offering rapid dynamic tracking, negligible steady-state oscillations under fast irradiance changes, and reduced online computational burden.

AI-driven MPPT approaches have been extensively surveyed and evaluated across diverse operating conditions [23]. Among these, fuzzy logic control offers a robust, parameter-independent, and fast-tracking framework [24]. To further enhance tracking precision under partial shading, adaptive fuzzy schemes often incorporate metaheuristics; for example, gray wolf optimization has been employed to dynamically tune FLC membership functions for optimal converter duty-cycle generation [25]. Artificial Neural Networks (ANNs) and hybrid schemes have also demonstrated rapid convergence under uniform irradiance to predict single MPP voltages in hardware implementations. Abouzeid et al. [26] validated a microcontroller-based multi-layer perceptron (MLP) network capable of fast power tracking under fluctuating radiation. To resolve tracking direction errors during fast cloud transients, Dawahdeh et al. [27] integrated local P&O logic with continuous neural network state estimation. Similarly, adaptive neuro-fuzzy inference systems

(ANFIS) have been applied to directly map temperature and irradiance measurements into optimal pulse width modulation (PWM) duty cycles for DC-DC boost converters [28]. More recently, deep reinforcement learning and deep predictive architectures have emerged to solve complex global tracking problems. Giraldo et al. [29] experimentally validated a deep Q-network framework designed for physical PV arrays under dynamic shading. Addressing tracking delays, Wadehra et al. [30] combined recurrent loops with policy-gradient methods to accelerate response times during sudden atmospheric shifts, while Yin et al. [31] proposed a deep predictive representation model that extracts latent shading features to make proactive duty-cycle adjustments before power drops occur.

To bridge the gap between rapid global tracking and steady-state precision, this paper presents a hybrid MPPT control framework integrating a feedforward neural network (FNN) with a standard P&O algorithm. The hybrid architecture leverages the rapid mapping capability of artificial neural networks to jump directly near the optimal operating region, followed by localized fine-tuning to suppress steady-state power ripple. In the proposed methodology, optimal duty cycles (D_{mpp}) corresponding to the GMPP are precalculated offline using the extracted PV model parameters across a comprehensive matrix of partial shading and thermal conditions. A three-layer FNN is trained on this dataset to establish a direct mapping from real-time environmental metrics (irradiance and temperature) to the target duty cycle. When environmental conditions change, the FNN immediately outputs a predicted D_{mpp}, enabling the converter operating point to move rapidly to the neighborhood of the GMPP, incorporating a threshold-guided progressive step transition mechanism that smoothly bridges the coarse neural prediction and fine-step local P&O tracking. Subsequently, a small-step P&O algorithm takes over to execute local tracking, correcting residual prediction errors and suppressing power oscillations. Comprehensive simulation studies validate that the proposed FNN-P&O scheme effectively mitigates transient oscillations, avoids local peak traps, and achieves fast convergence to the GMPP under dynamic partial shading scenarios.

2. Identification of a PV Cell

To simulate a PV cell, the standard single-diode model (also known as the 5-parameter model) is widely used because it offers an excellent balance between accuracy and simplicity. In this section, we develop the mathematical formulation of the single-diode model.

2.1. Equivalent Circuit Model

The single-diode model consists of a photocurrent source, one diode representing the p-n junction diffusion mechanisms, a shunt resistor (R_{sh}) accounting for leakage current, and a series resistor (R_s) representing internal resistance. Figure 1 shows the single-diode equivalent circuit model of a PV cell.

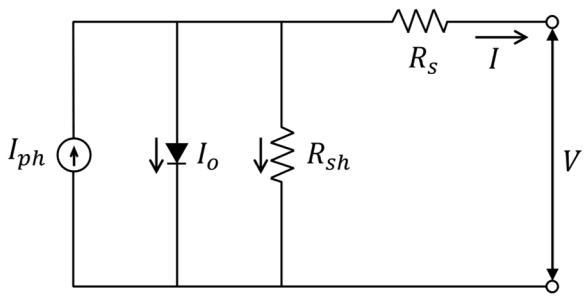

Figure 1. Equivalent circuit of a PV cell based on the single-diode model [1,2,32].

The output current I of the PV cell is governed by the following implicit nonlinear equation [1,2,32]:

$$I = I_{ph} - I_o\left[\exp\left(\frac{V + IR_s}{aV_t}\right) - 1\right] - \frac{V + IR_s}{R_{sh}}, \quad (1)$$

where V and I are the output voltage (V) and current (A) of the PV cell, respectively, I_{ph} is the photocurrent or light-generated current (A), I_o is the diode reverse saturation current (A), R_s is the series resistance (Ω), R_{sh} is the shunt resistance (Ω), a is the diode ideality factor, K is the Boltzmann constant (1.38065×10^{-23} J/K), q is the electron charge (1.60218×10^{-19} C), T is the cell temperature in Kelvin (K), and $V_t = KT/q$ is the thermal voltage.

To capture dynamic environmental variations, the model updates its parameters in response to changing solar irradiance (G) and cell temperature (T). The photocurrent (I_{ph}) is expressed as

$$I_{ph} = \frac{G}{G_n}\left[I_{ph,n} + K_I(T - T_n)\right], \quad (2)$$

where G_n is the nominal irradiance (1000 W/m^2), T_n is the nominal temperature (25 °C), I_{ph}, n is the nominal light current (often approximated by the short-circuit current I_{sc}) and K_I is the short-circuit current temperature coefficient (A/K). The saturation current (I_o) is calculated as

$$I_o = I_{o,n}\left(\frac{T}{T_n}\right)^3 \exp\left[\frac{qE_g}{aK}\left(\frac{1}{T_n} - \frac{1}{T}\right)\right], \quad (3)$$

where $I_{o,n}$ is the nominal saturation current, calculated from open-circuit conditions and E_g is the bandgap energy of the semiconductor.

If we consider an entire PV module consisting of N_s cells connected in series and N_p cells in parallel, the characteristic equation is as follows:

$$I = I_{ph}N_p - I_oN_p\left[\exp\left(\frac{V + \frac{N_s}{N_p}IR_s}{N_saV_t}\right) - 1\right] - \frac{V + \frac{N_s}{N_p}IR_s}{\frac{N_s}{N_p}R_{sh}}, \quad (4)$$

This nonlinear equation contains current (I) on both sides. It can be solved either analytically using the Lambert W function or numerically. Equation (4) is rewritten by

$$f(V, I, \theta) = I_{ph}N_p - I_oN_p\left[\exp\left(\frac{V + \frac{N_s}{N_p}IR_s}{N_saV_t}\right) - 1\right] - \frac{V + \frac{N_s}{N_p}IR_s}{\frac{N_s}{N_p}R_{sh}} - I = 0, \quad (5)$$

where $\theta = \left[I_{ph}, I_o, a, R_s, R_{sh}\right]^T$ is the unknown parameter vector. Figures 2 and 3 present the *I-V* and *P-V* characteristics of the PV cell under two conditions: varying solar irradiance (G) at a constant temperature ($T = 25$ °C), and varying temperature (T) at a constant irradiance ($G = 1000$ W/m^2).

As depicted in Figures 2 and 3, the maximum power output is highly sensitive to solar irradiance variations, but it remains relatively stable across temperature variations.

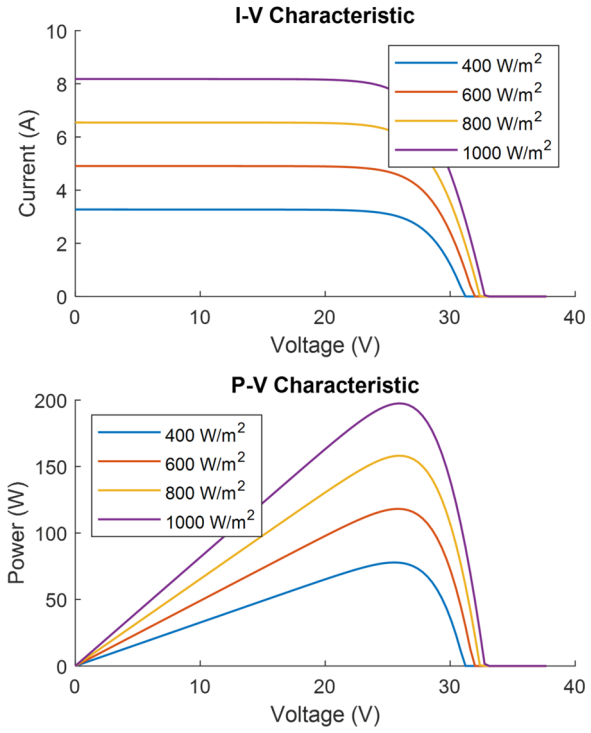

Figure 2. *I-V* and *P-V* characteristics under varying G under a constant $T = 25$ °C.

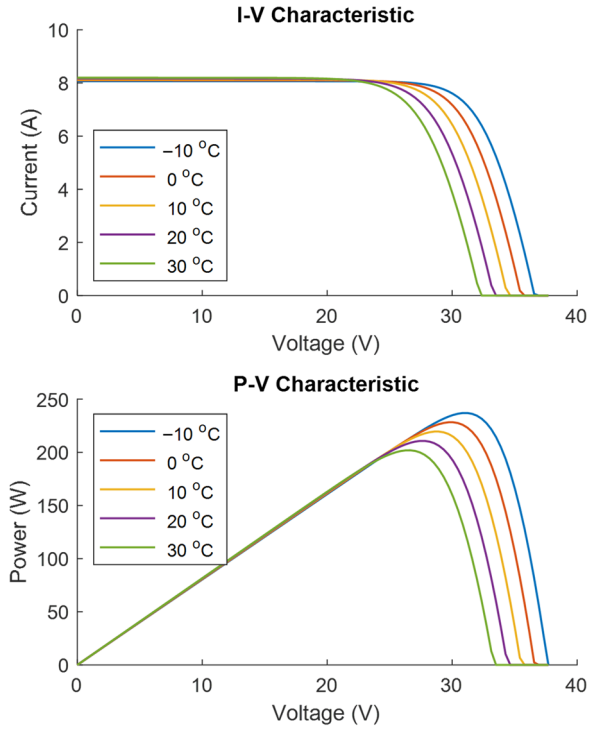

Figure 3. *I-V* and *P-V* characteristics under varying T under a constant $G = 1000$ W/m².

2.2. Parameter Estimation of a PV Cell

Following model definition and input/output data (V, I) taken from the manufacturer's datasheet [33], the unknown parameters are estimated. The simulated estimation targets a single Kyocera KC200GT module under Standard Test Conditions (STCs): irradiance $G = 1000$ W/m², cell temperature $T = 25$ °C, and air mass $AM = 1.5$. The datasheet ratings for this panel are $P_{max} = 200$ W, $V_{max} = 26.3$ V, $I_{max} = 7.61$ A, $V_{oc} = 32.9$ V, $I_{sc} = 8.21$ A with a connection of $N_s = 54$ and $N_p = 1$ [33,34]. Note that $I_{ph} = I_{ph,n}$ and

$I_o = I_{o,n}$ at STCs. Equation (4) has five unknown parameters: I_{ph}, I_o, a, R_s, and R_{sh}. When estimating them, performance indices (or objective functions) serve as quantitative metrics to evaluate the accuracy, fidelity, and convergence of optimization algorithms. These metrics quantify the discrepancy between datasheet *I-V* characteristic data and model-simulated values. Given a data set of V_k and I_k, calculate the root mean square error (RMSE) index:

$$\text{RMSE} = \sqrt{\frac{1}{M}\sum_{k=1}^{M} f^2(V_k, I_k, \theta)}\,, \tag{6}$$

where V_k and I_k are the kth datasheet voltage and current of the PV module, respectively and M is the total number of data points. To solve the resulting multivariate optimization problem, the hybrid genetic algorithm (HGA) utilizing affine combination-based reproduction and non-uniform mutation is employed [35]. Setting N_s = 54 in Equation (5) ensures that the extracted parameters correspond to a single PV cell rather than a complete PV module.

By connecting the estimated model in series or parallel using bypass diodes, GMPP values under various environmental conditions are numerically calculated and subsequently used to train a neural network predictor covered in the following section.

3. MPPT Control of PV Modules

PV cells function as nonlinear power sources. For any specific irradiance and cell temperature, maximum power output (P_{max}) occurs at a single operating point. Deviating even slightly from this optimal point causes a sharp drop in energy yield. Solar radiation directly influences current—and thus peak power—while passing clouds trigger rapid power fluctuations. Temperature also plays a critical role: as cells heat up, open-circuit voltage (V_{oc}) decreases, shifting the MPP to a lower voltage. Under PSCs, the *P-V* curve develops multiple local peaks. Dynamic MPPT control is therefore essential to continuously track the GMPP and eliminate avoidable power loss.

Non-uniform irradiance across three series-connected modules generates up to three distinct local maxima on the *P–V* curve due to the interaction between non-uniform irradiance (partial shading) and the bypass diodes [36], as shown in Figure 4. Shifts in irradiance ratios activate or deactivate bypass diodes, causing abrupt jumps in the GMPP location. When scaling to n modules, the number of potential local peaks increases up to n. Even for a single module, partial shading of its cell sub-strings, each protected by its own bypass diode, produces similar multi-peak *P-V* characteristics. Across the evaluated scenarios, the operational parameters vary significantly: Figure 4a yields V_{mpp} = 78.189 V, I_{mpp} = 7.606 A, and P_{max} = 594.718 W; Figure 4b gives V_{mpp} = 24.771 V, I_{mpp} =7.574 A, and P_{max} = 187.605 W; Figure 4c shows V_{mpp} = 52.815 V, I_{mpp} = 6.290 A, and P_{max} = 332.193 W; Figure 4d provides V_{mpp} = 83.020 V, I_{mpp} = 4.778 A, and P_{max} = 396.687 W. This multi-peak behavior explains why conventional MPPT algorithms frequently get trapped in a local optimum.

To address these challenges and ensure optimal performance under dynamic conditions, we propose a system architecture shown in Figure 5. This system comprises six primary components: a PV string, a boost converter, an FNN, a hybrid fast-tracking P&O algorithm, sensors, and a load. The designed components are detailed in the following section.

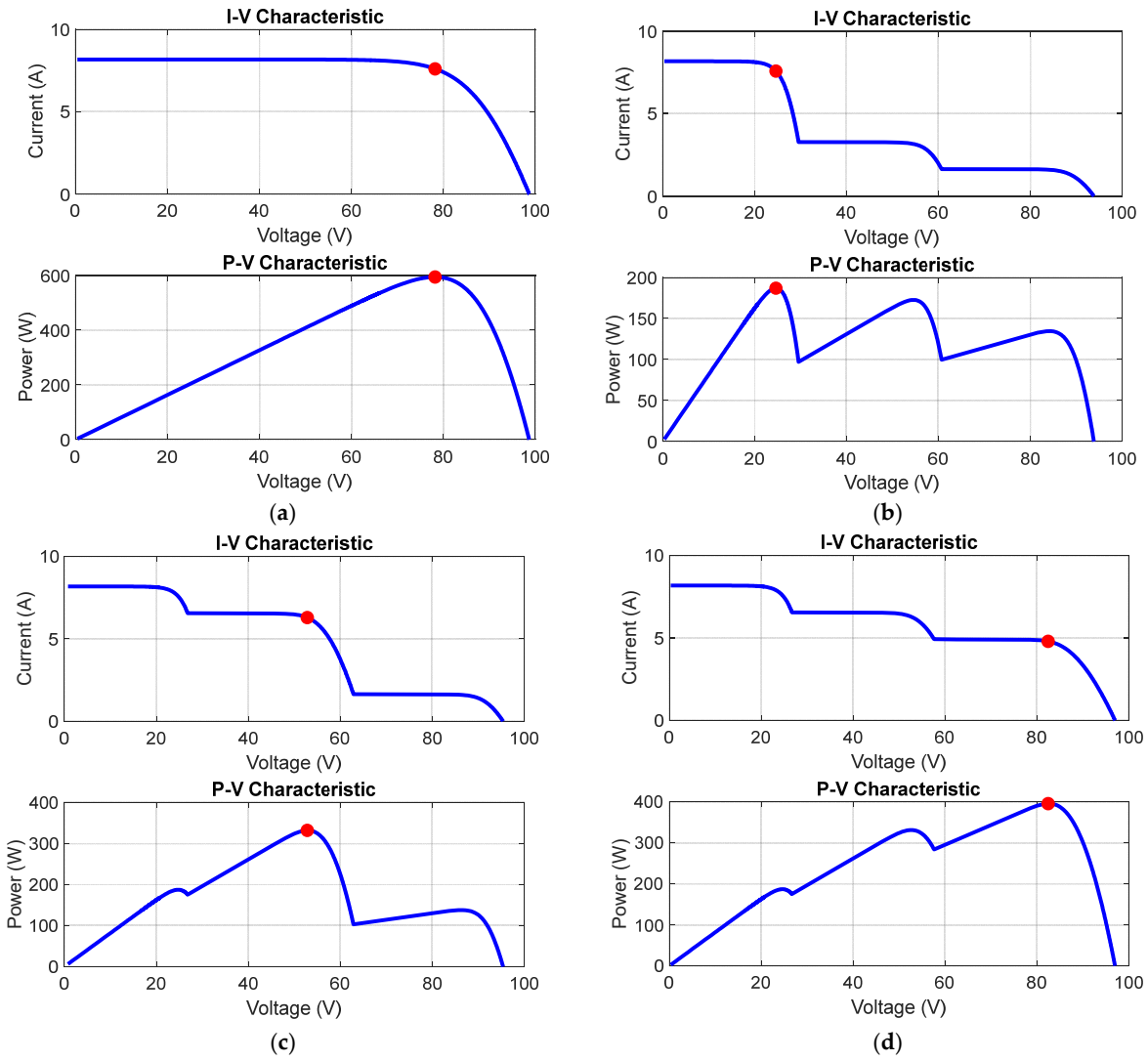

Figure 4. *I-V* and *P-V* characteristics of three series-connected modules under uniform or non-uniform irradiance profiles: (**a**) $G = [1000, 1000, 1000]$ W/m^2. (**b**) $G = [1000, 200, 400]$ W/m^2. (**c**) $G = [1000, 200, 800]$ W/m^2. (**d**) $G = [1000, 600, 800]$ W/m^2.

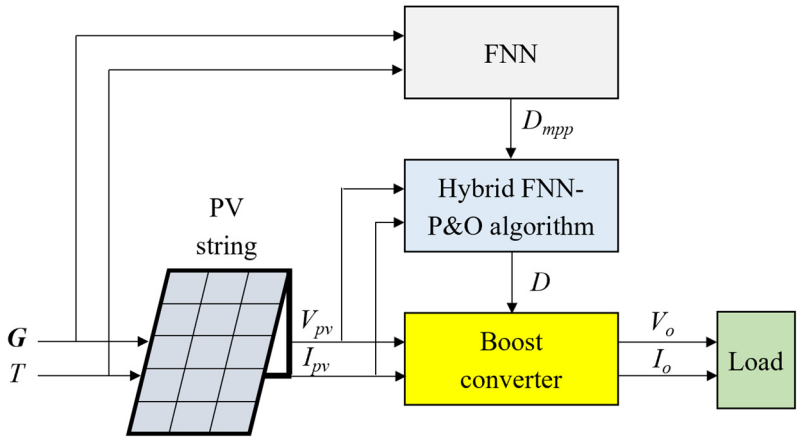

Figure 5. Block diagram of the hybrid FNN-P&O controller for PV MPPT.

3.1. Boost Converter Design

A boost converter is a switched-mode DC-to-DC power converter that increases an input voltage (V_{pv}) to a higher output voltage (V_o) while supplying power efficiently to a

load. Because power is conserved ($P_{pv} \approx P_o$), increasing output voltage causes a proportional decrease in output current ($I_o < I_{pv}$) and vice versa. A basic non-isolated boost converter relies on five key components to manage power transfer: an inductor for energy storage, a MOSFET switch for high-frequency control, a diode for directional valve, an output capacitor for smoothing & reservoir and a PWM controller for feedback & regulation. For filtering input ripple voltage, an input capacitor (C_{in}) can be placed in parallel across the input DC supply rails before the main inductor.

To size the power stage components (L, C_{in}, C_{out}), establish standard operational baseline parameters:

- Switching frequency (f_s): 50 kHz;
- Nominal output voltage (V_o): 150 V, used for component rating and sizing (for the 3-module string, $V_{oc,string} \approx 98.7$ V under STC);
- Target inductor current ripple (ΔI_L): 30% of maximum input current (0.3 × 7.61 A = 2.28 A);
- Target voltage ripple: $\Delta V_{pv} \leq 0.5\%$ (0.4 V), $\Delta V_o \leq 1.0\%$ (1.5 V).

3.1.1. Duty Cycle (D)

Using the ideal boost converter relationship $D = 1 - V_{pv}/V_o$:

$$D_{min} = 1 - \frac{78.9\ \text{V}}{150\ \text{V}} = 0.474 \quad (G = 1000\ \text{W/m}^2), \tag{7}$$

$$D_{max} = 1 - \frac{73.5\ \text{V}}{150\ \text{V}} = 0.510 \quad (G = 200\ \text{W/m}^2). \tag{8}$$

3.1.2. Equivalent Load Resistance (R)

Assuming a 3-module string operating at the nominal output voltage of 150 V with an output efficiency (η) of 95% to 100% ($P_o = V_o^2/R$):

- Full irradiance ($G = 1000\ \text{W/m}^2$, $P_o = 600$ W):

$$R_{min} = \frac{V_o^2}{P_o} = \frac{150^2}{600} = 37.5\ \Omega. \tag{9}$$

- Low irradiance ($G = 200\ \text{W/m}^2$, $P_o = 112$ W):

$$R_{max} = \frac{V_o^2}{P_o} = \frac{150^2}{112} = 200.9\ \Omega. \tag{10}$$

Because the converter feeds a fixed resistive load, Vo is not regulated but varies with the extracted power as $V_o = \sqrt{P_o \cdot R}$. A fixed load of $R = 40\ \Omega$ was used in all simulations.

3.1.3. Inductor (L)

The minimum inductance needed to bound peak-to-peak current ripple $\Delta I_L \leq 2.28$ A at $1000\ \text{W/m}^2$:

$$L = \frac{V_{pv} \cdot D}{\Delta I_L \cdot f_s} = \frac{78.9\ \text{V} \times 0.474}{2.28\ \text{A} \times 50\ \text{kHz}} = 328\ \mu\text{H}, \tag{11}$$

Critical Inductance Check for Continuous Conduction Mode (CCM) at 200 W/m^2 ($I_{mpp} = 1.52$ A):

$$L_{critical} = \frac{V_{pv} \cdot D}{2 \cdot I_{mpp} \cdot f_s} = \frac{73.5\ \text{V} \times 0.510}{2 \times 1.52\ \text{A} \times 50\ \text{kHz}} = 246.6\ \mu\text{H}. \tag{12}$$

Since $L > L_{critical}$, selecting $L = 470$ µH ensures CCM across the entire irradiance range with margin.

3.1.4. Input Capacitor (C_{in})

C_{in} buffers switching ripple and decouples MPPT voltage perturbations. Its size is based on the allowable input voltage ripple ΔV_{in}, the inductor ripple current ΔI_L, and the switching frequency f_s.

- High-frequency switching ripple requirement ($\Delta V_{in} \leq 0.4$ V):

$$C_{in,min} = \frac{\Delta I_L}{8 \cdot f_s \cdot \Delta V_{in}} = \frac{2.28\ \text{A}}{8 \times 50\ \text{kHz} \times 0.4\ \text{V}} = 14.25\ \mu\text{F}. \quad (13)$$

- MPPT dynamic stability requirement: To prevent tracking oscillations caused by V_{pv} collapse during P&O steps, low-ESR electrolytic/film capacitors are required: C_{in} = 200 µF to 470 µF.

3.1.5. Output Capacitor (C_o)

During switch ON-time, C_o supplies the full output load current (I_o = 600 W/150 V = 4 A).

- High-frequency output ripple requirement ($\Delta V_o \leq 1.5$ V):

$$C_{o,min} = \frac{I_o \cdot D}{f_s \cdot \Delta V_o} = \frac{4\ \text{A} \times 0.474}{50\ \text{kHz} \times 1.5\ \text{V}} = 25.28\ \mu\text{F}. \quad (14)$$

- Transient load & MPPT perturbation requirement: To absorb output power fluctuations without voltage collapse: Recommended C_o = 220 µF to 470 µF.

3.1.6. Prediction of a Duty Cycle at MPP

According to the maximum power transfer theorem, maximum power is delivered to a load when the source's internal impedance matches the load impedance. Because a PV module's equivalent internal impedance fluctuates continuously with environmental conditions and load variations, directly connecting it to a fixed load causes severe impedance mismatch. An MPPT controller functions as an adaptive DC-DC converter that dynamically adjusts its duty cycle (D) to match the reflected load impedance with the PV source's optimal internal resistance. Real-time measurements of V_{pv} and I_{pv}, combined with a known load resistance R, enable the implementation of a hybrid feedforward MPPT control strategy using V_{mpp}. On the input side, the solar panel operates at V_{mpp} and supplies I_{mpp}. Assuming 100% converter efficiency, the total output power delivered to the load is $P_{max} = V_{mpp} \times I_{mpp}$, which uniquely determines the load voltage and current for a fixed R. In this configuration, the boost converter functions as an impedance matching network, forcing the PV panel to maintain peak power operation. The equivalent input resistance presented to the panel (R_{pv}) is related to the load resistance by

$$R_{pv} = \frac{V_{pv}}{I_{pv}} = (1 - D)^2 R, \quad (15)$$

Solving for D gives

$$D = 1 - \sqrt{\frac{V_{pv}}{I_{pv} \cdot R}}, \quad (16)$$

To ensure the solar panel operates at its MPP where $R_{mpp} = V_{mpp}/I_{mpp}$, the predicted duty cycle is calculated as

$$D_{mpp} = 1 - \sqrt{\frac{V_{mpp}}{I_{mpp} \cdot R}}. \quad (17)$$

3.2. Hybrid Fast-Tracking P&O Algorithm

3.2.1. NN-Based MPP Duty Cycle Predictor

In this study, the operating conditions for the PV string—comprising three series-connected modules—are defined within $200\ \mathrm{W/m^2} \le G \le 1000\ \mathrm{W/m^2}$ and $0\ ^\circ\mathrm{C} \le T \le 30\ ^\circ\mathrm{C}$. The string parameters (V_{mpp} and I_{mpp}) are calculated using Equation (4), while the predicted duty cycle at the MPP is determined from Equation (17). Building upon the preceding analysis of environmental impacts on D_{mpp}, these nonlinear input–output relationships are mapped using neural network architectures. FNNs are well-suited for this task due to their backpropagation learning mechanism, robust handling of nonlinear dynamics, and strong universal approximation capabilities—theoretically guaranteeing that an FNN can approximate any continuous function with arbitrary accuracy.

The proposed architecture employs a three-layer Multi-Layer Perceptron (MLP) comprising an input layer, two hidden layers, and an output layer to map $[G_1,\ G_2,\ G_3,\ T]$ to D_{mpp}. Figure 6 illustrates its structure.

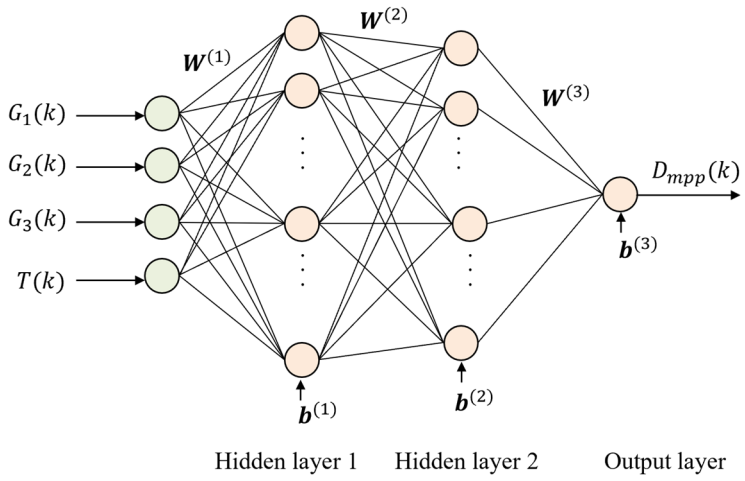

Figure 6. Structure of a three-layer FNN.

The input vector $\boldsymbol{x} = [G_1, G_2, G_3, T]^T \in \mathbb{R}^4$ is passed directly to the first hidden layer without applying any weights. The network contains two hidden layers with m_1 and m_2 nodes, respectively. Each node computes a weighted linear combination of its inputs, adds a bias term, and applies a nonlinear activation function. The final hidden layer responses are combined in the output layer—typically using a linear activation function—to produce the scalar output $y = D_{mpp} \in \mathbb{R}$. The signal propagation through the NN layer structure is defined as

$$\begin{aligned} \boldsymbol{h}_1 &= f_1(\boldsymbol{W}^{(1)} \cdot \boldsymbol{x} + \boldsymbol{b}^{(1)}), \\ \boldsymbol{h}_2 &= f_2(\boldsymbol{W}^{(2)} \cdot \boldsymbol{h}_1 + \boldsymbol{b}^{(2)}), \\ y &= \boldsymbol{W}^{(3)} \cdot \boldsymbol{h}_2 + \boldsymbol{b}^{(3)}, \end{aligned} \tag{18}$$

where $\boldsymbol{W}^{(1)}$, $\boldsymbol{W}^{(2)}$, and $\boldsymbol{W}^{(3)}$ denote the interconnection weight matrices; $\boldsymbol{h}_1$ and $\boldsymbol{h}_2$ represent the post-activation signal vectors of the first and second hidden layers; $\boldsymbol{b}^{(1)}$, $\boldsymbol{b}^{(2)}$, and $\boldsymbol{b}^{(3)}$ represent the corresponding bias vectors (or scalars). The non-linear activation functions for the hidden layers are denoted by $f_1(\cdot)$ and $f_2(\cdot)$, typically chosen as hyperbolic tangent sigmoid functions.

3.2.2. Fast-Tracking P&O Algorithm

Incorporating the PV panel measurements $V(k)$ and $I(k)$ together with the neural-network-predicted duty cycle $D_{mpp}(k)$ at step k, the proposed MPPT control scheme

operates according to the flowchart in Figure 7. To achieve both rapid transient tracking and minimal steady-state power ripple, the algorithm seamlessly transitions between two distinct operational modes:

- FNN-based fast-tuning mode: When a significant shift in solar irradiance or temperature occurs, the operating point deviates from $D_{mpp}(k)$, requiring a duty cycle update. Direct, sudden adjustments can induce abrupt voltage and current transients in power converters, potentially triggering over-voltage/over-current protections or destabilizing the control loop. Updating D progressively via fixed coarse steps rapidly moves the operating point toward the optimal region without overshooting the target duty cycle, enabling a seamless transition into the fine-tuning mode to minimize steady-state oscillation. Therefore, we calculate the duty cycle error $e_D(k) = D_{mpp}(k) - D(k-1)$. If $|e_D(k)|$ exceeds a predefined threshold TH, the duty cycle updates via:

$$D(k) = D(k-1) + \text{sign}\big(e_D(k)\big) \times \Delta D_{coarse}, \tag{19}$$

where sign(·) is the sign function, returning either +1, −1, or 0 and ΔD_{coarse} is the fast step size for duty cycle perturbation. The relatively large step size rapidly drives the system toward the target duty cycle.

- Fine-tuning mode: Once $D(k)$ is sufficiently close to $D_{mpp}(k)$ $(|e_D(k)| \le TH)$, flow control is back to the standard P&O algorithm using a fine step size. This significantly suppresses steady-state oscillations and compensates for any residual error between NN prediction and the real GMPP. Finally, the updated duty cycle $D(k)$ is constrained within saturation limits of $D_{min} = 0.05$ and $D_{max} = 0.95$.

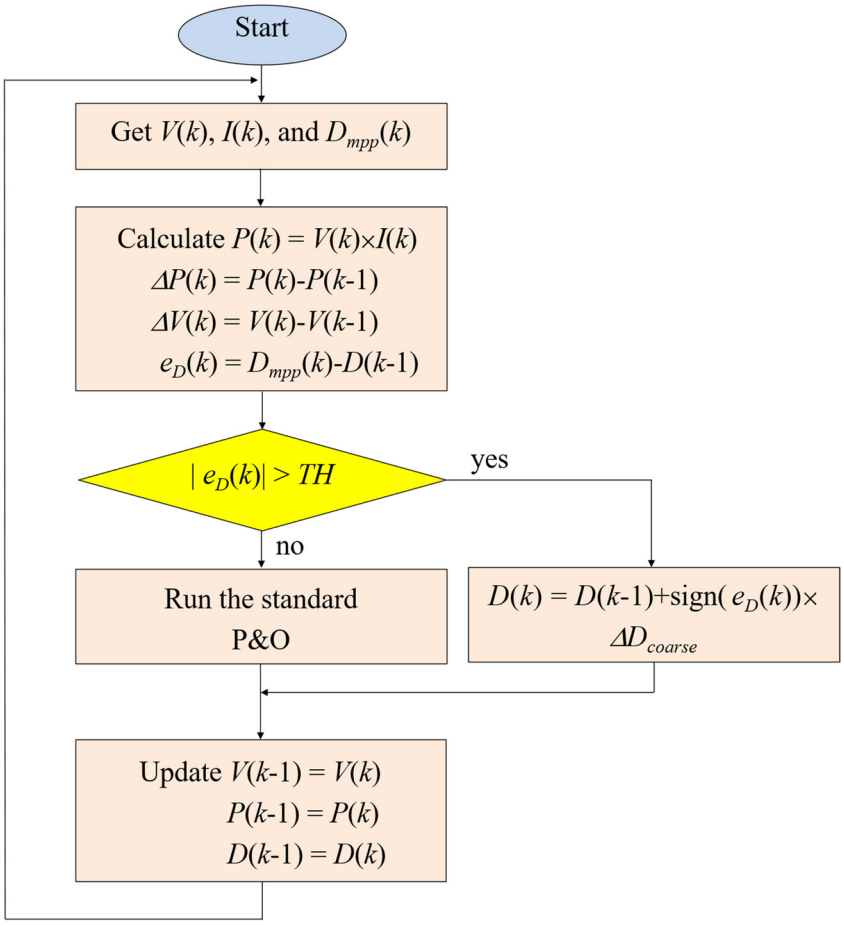

Figure 7. Flow chart of the proposed MPPT algorithm.

Because $e_D(k)$ is evaluated at every control step, no separate environmental-change detector is required: any change in G or T is immediately reflected in $D_{mpp}(k)$ and hence in $|e_D(k)|$, which automatically activates the fast-tuning mode when $|e_D(k)| > TH$.

3.3. Sensors

In photovoltaic (PV) systems, module-level irradiances (G_1, G_2, G_3) and cell temperature (T) are commonly acquired using dedicated sensors. In practical installations, irradiance can be measured via surface-mounted pyranometers or photodiode sensors, while temperature is monitored using back-of-module RTDs or thermocouples. Alternatively, sensorless estimation techniques—such as deploying pilot PV cells or deriving irradiance directly from open-circuit voltage and short-circuit current measurements—can be employed to reduce hardware costs. In this study, the proposed method is evaluated through simulations, assuming these environmental parameters are known *a priori*.

4. Simulation and Discussion

To verify the efficacy of the proposed method, simulations were conducted in MATLAB/Simulink R2026a (MathWorks, Natick, MA, USA) using its Simscape and Deep Learning Toolboxes [37,38]. Figure 8 shows the Simulink model of the FNN-P&O MPPT scheme. The overall model comprises varying environmental inputs (G_1, G_2, G_3, T), three series-connected PV modules each with a bypass diode, an FNN predictor, a P&O algorithm block, a PWM generator and a power stage circuit feeding the load. At the network input stage, dedicated blocks normalize the environmental signals before combining them into a 1 × 4 input vector. The parameters of the DC-DC converter are set according to the design values established in the previous section.

The performance of the proposed hybrid FNN-P&O method was evaluated across five test scenarios and benchmarked against both standard and adaptive P&O algorithms. For the FNN-P&O scheme, the fine step size was set to 0.00005, while the coarse step size (ΔD_{coarse}) and threshold (TH) were both set to 0.05—enabling the system operating point to quickly converge toward the target duty cycle without overshooting. The threshold and step size were determined through extensive trial and error. The standard P&O method used a fixed step size of 0.0005. For the adaptive P&O algorithm [12], which dynamically adjusts the perturbation step size via $\Delta D(k) = \alpha|\Delta P/\Delta V|$, α was empirically set to a value of 0.002 to prevent local trap, with bounds defined as ΔD_{min} = 0.0001 and ΔD_{max} = 0.0015.

Tracking performance is assessed using three key quantitative metrics: percentage overshoot (M_p), overall MPPT efficiency (η_{mpp}), and absolute energy loss (E_{loss}) defined as:

$$\eta_{mpp} = \frac{\sum_{k=1}^{M} P_{pv}(k)}{\sum_{k=1}^{M} P_{mpp}(k)} \times 100\ \% \tag{20}$$

$$E_{loss} = \sum_{k=1}^{M} |P_{mpp}(t) - P_{pv}(t)| \cdot \Delta t \tag{21}$$

where $P_{mpp}(k)$ is the theoretical maximum power available from the PV array under instantaneous ambient conditions, $P_{pv}(k)$ is the actual output power measured at the PV array terminals and M is the total number of data samples. The percentage overshoot M_p is defined as the maximum absolute deviation of P_{pv} from the steady-state GMPP power after an environmental change, normalized by that value (×100%); for downward irradiance steps, it represents the depth of the transient power dip.

Hereafter, the proposed FNN-P&O MPPT control scheme for the PV-fed boost converter is referred to as "FNN-P&O", the standard P&O MPPT scheme as "P&O" and the adaptive P&O MPPT scheme as "AP&O".

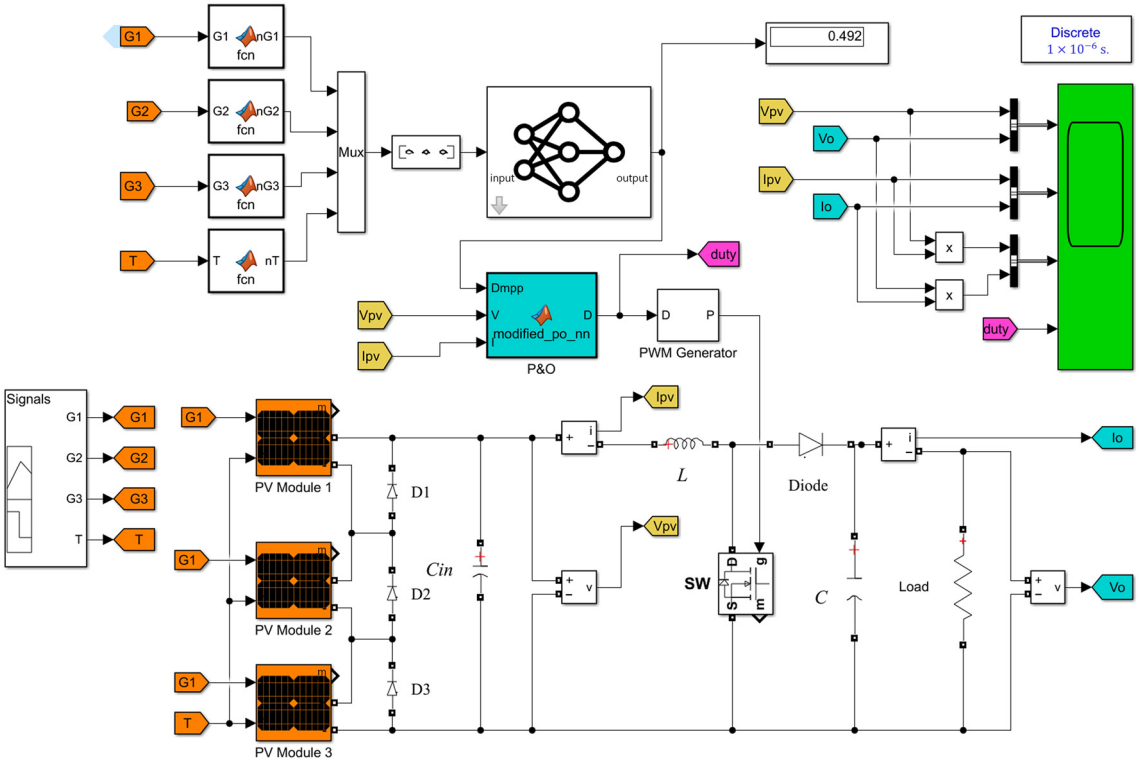

Figure 8. Simulink model of the FNN-P&O MPPT scheme for the PV-fed boost converter system.

4.1. Parameter Estimation of a Kyocera KC200GT Cell

Under STCs, parameter estimation of a PV cell involves extracting unknown electrical parameters from equivalent circuit models to accurately match datasheet *I-V* characteristic curves. For the HGA, the parameters are configured as follows: a population size of $N = 40$; reproduction settings with $\eta = 1.8$ and $\sigma = 0.01$; non-uniform mutation probability $P_m = 0.04$ and $b = 6$ [35]. The maximum number of generations was set to 4000. The search bounds were defined by the lower bound $\boldsymbol{x}^{(L)} = [0, 0, 0, 0, 0]^T$ and the upper bound $\boldsymbol{x}^{(U)} = [20, 0.1, 5, 1, 300]^T$. Since the HGA's convergence capability and performance depend on its initial population, 20 independent runs were executed with distinct random seeds to ensure reliable parameter estimation. The mean estimated parameters across these runs are summarized in Table 1.

Table 1. Parameter estimates of the single-diode model.

Parameter	Symbol (Unit)	Estimate
Photodiode current	I_{ph} (A)	8.179 ± 0.017
Reverse saturation current	I_o (μA)	0.073 ± 0.033
Ideality factor	a	1.274 ± 0.113
Series resistance	R_s (Ω)	0.005 ± 0.001
Shunt resistance	R_{sh} (Ω)	144.053 ± 1.184

The estimated model was validated by plotting the simulated *I-V* and *P-V* characteristic curves against the datasheet *I-V* characteristic data points (red circles) in Figure 9. The coefficient of determination (R^2) was utilized to assess the model's accuracy in reproducing the datasheet I–V characteristics as:

$$R^2 = 1 - \frac{\sum_{j=1}^{M} \left(I_j - I_{est,j}\right)^2}{\sum_{j=1}^{M} \left(I_j - \bar{I}_{datasheet}\right)^2}, \tag{22}$$

where $\bar{I}_{datasheet}$ is the average value of the datasheet I. The agreement is confirmed by an R-squared value of 99.96%, indicating a high fitting accuracy between the HGA-based estimated parameters and the datasheet data.

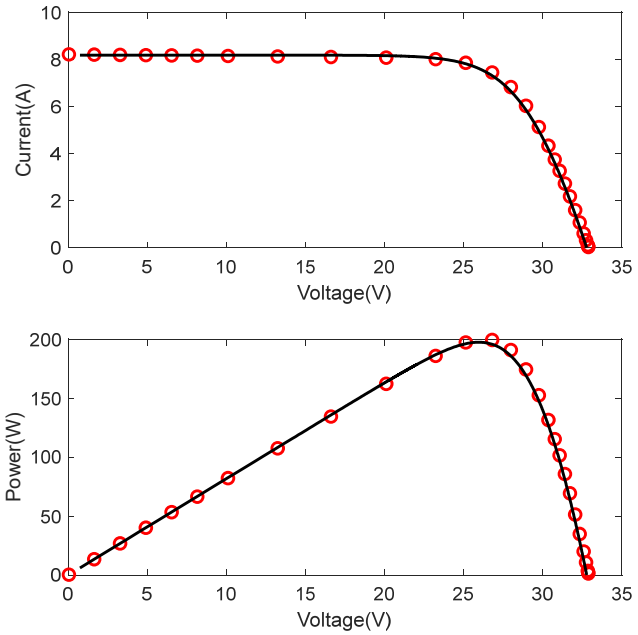

Figure 9. Datasheet I-V data points and I-V and P-V characteristics curves of the estimated model.

4.2. FNN Data Generation and Training

We simulated D_{mpp} under varying environmental conditions by sweeping solar irradiance from 200 W/m^2 to 1000 W/m^2 in steps of 10 W/m^2 and cell temperature from 0 °C to 30 °C in steps of 2 °C. Under the assumption of isothermal conditions across the three modules, Figure 10 depicts the four-dimensional volumetric parameter distributions of a string comprising three series-connected PV modules with bypass diodes, obtained via Equations (4) and (17).

Under PSCs, bypass diodes activate or deactivate depending on irradiance differences among modules. This triggers abrupt shifts in the MPP, resulting in sharp step changes and near-discontinuities across the V_{mpp} and I_{mpp} mapping surfaces. Although V_{mpp} and I_{mpp} undergo discrete inverse jumps, their product P_{max} transitions smoothly across shading states as shown in Figure 10c. However, D_{mpp} inherits the sharp piecewise-continuous regions induced by bypass diode switching.

To reduce computational load during Simulink simulation, network training data were sampled at step sizes of ΔG = 200 W/m^2 across irradiance levels from 200 to 1000 W/m^2 and ΔT = 10 °C across temperatures from 0 to 30 °C. Using the sampled data, D_{mpp} was subsequently computed according to Equation (17). This yielded a training dataset comprising $M \times 4$ inputs and $M \times 1$ target output, where M = 500. The dataset was split 70/15/15% into training, validation, and test sets, and the network with m_1 = 40 and m_2 = 20 hidden nodes was trained using MATLAB's Deep Learning Toolbox with the Adam optimizer (learning rate 0.001, 10,000 epochs) [37]. Figure 11 shows the learning trajectory, in which the training RMSE converged to 1×10^{-4}, whereas the validation RMSE settled at 0.068, mainly owing to the near-discontinuous changes in D_{mpp} at bypass-diode transition boundaries under the

coarse sampling grid. This accuracy is sufficient for the proposed scheme, since the FNN only needs to bring the operating point near the GMPP, after which the fine-step P&O removes the residual error, as confirmed by Scenario 4 in Section 4.3.

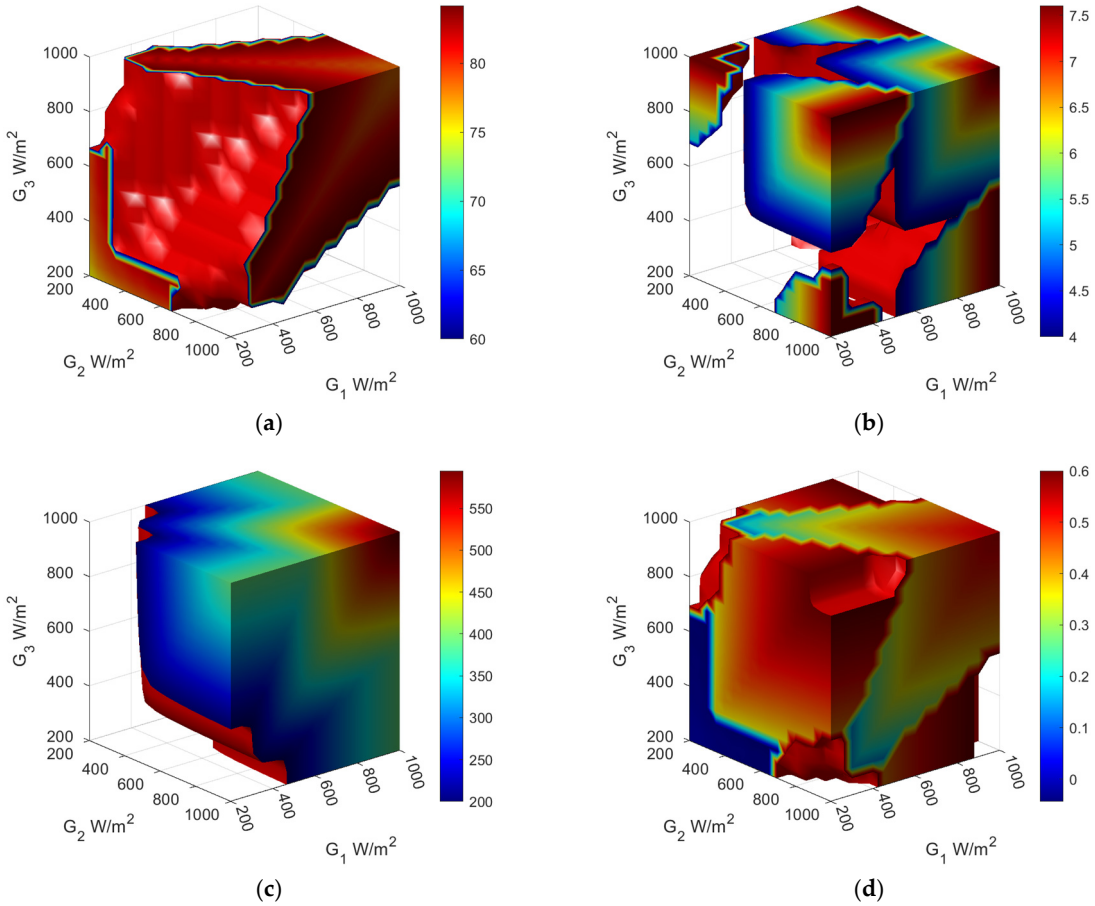

Figure 10. Four-dimensional plots of PV string parameters across the irradiance domain (G_1, G_2, G_3) at $T = 25$ °C: (**a**) Maximum power point voltage V_{mpp}. (**b**) Maximum power point current I_{mpp}. (**c**) Maximum power P_{max}. (**d**) Estimated duty cycle D_{mpp}.

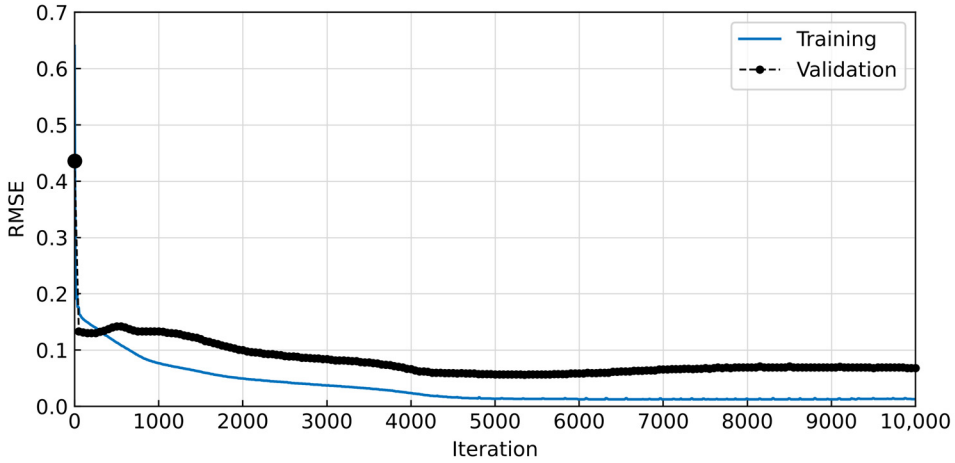

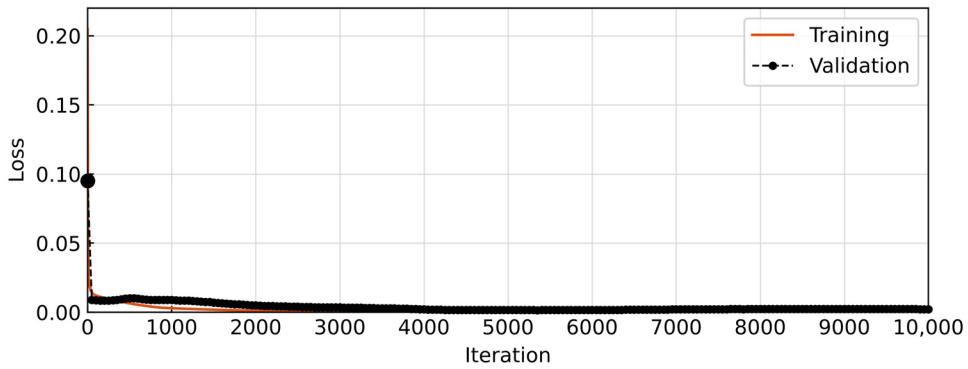

Figure 11. Learning process of the network for predicting D_{mpp}.

4.3. MPPT Performance Test

4.3.1. Scenario 1: STCs

The tracking performances of the three methods were evaluated under STCs. As shown in Figures 12 and 13, the simulation was conducted over a duration of 0.5 s.

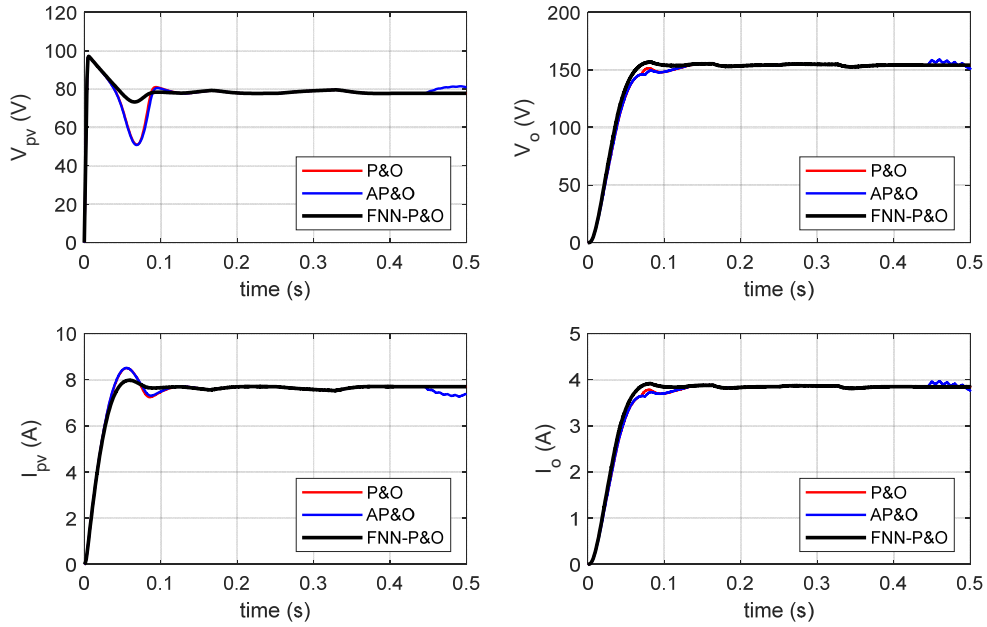

Figure 12. Dynamic response comparison of V_{pv}, I_{pv}, V_o and I_o for the P&O, AP&O, and FNN-P&O methods under STCs.

In Figure 12, the top two plots show the PV panel and output terminal voltages, while the remaining plots show their corresponding currents. The top two plots in Figure 13 depict the power at the PV panel and output terminals, respectively, while the others show the duty cycles. In Scenario 1 where a single power peak exists, the three methods successfully track the global peak, producing around 600 W within 0.1 s. However, the P&O and AP&O methods exhibit a significant power dip down to approximately 400 W between t = 0.05 s and t = 0.1 s. This reflects the inherent tracking drift or directional confusion during rapid operating point shifts or perturbation steps. The FNN-P&O method significantly improves dynamic tracking stability by eliminating the large transient power loss seen in the P&O-based methods during initial tracking, ensuring higher energy extraction efficiency without sacrificing convergence speed. A quantitative comparison between the three methods under STCs is summarized in Table 2.

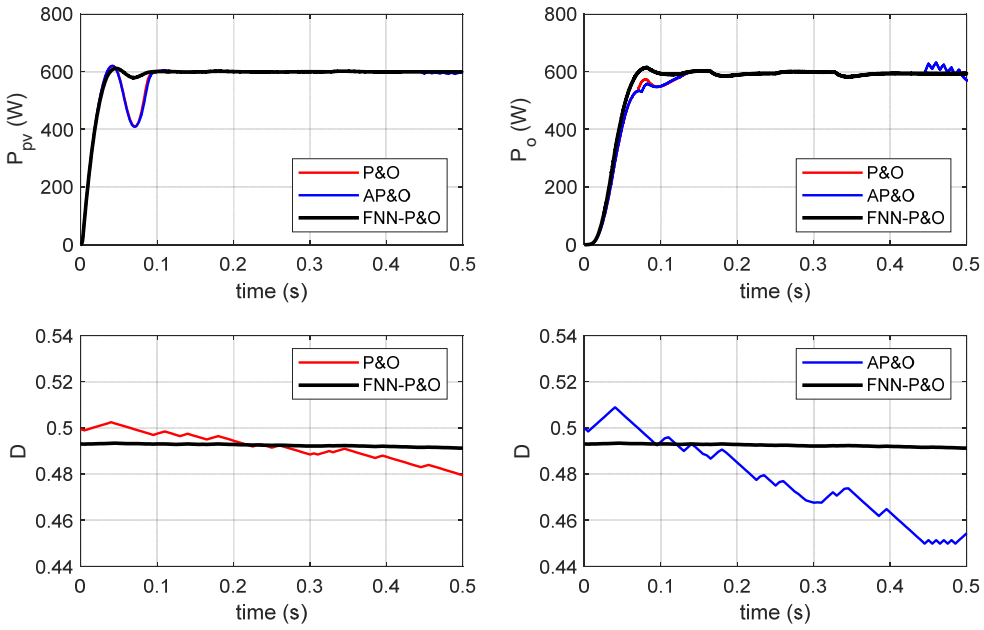

Figure 13. Dynamic response comparison of P_{pv}, P_o and D for the P&O, AP&O, and FNN-P&O methods under STCs.

Table 2. Quantitative performance metrics of the three methods under STCs.

Method	Performance Metric		
	M_p (%)	η_{mpp} (%)	E_{loss} (J)
P&O	3.35	95.51	14.14
AP&O	3.37	95.36	14.59
FNN-P&O	1.94	96.85	9.90

The proposed FNN-P&O method demonstrates superior overall performance, achieving the lowest overshoot of 1.94% compared to 3.35% for conventional P&O and 3.37% for AP&O. Furthermore, FNN-P&O achieves the highest tracking efficiency at 96.85%, while significantly reducing the absolute energy loss to 9.90 J, representing a substantial improvement over P&O (14.14 J) and AP&O (14.59 J). This corresponds to reductions in energy loss of approximately 30.0% and 32.1% relative to P&O and AP&O, respectively.

4.3.2. Scenarios 2–4: PSCs

For the next simulation, the tracking capability of the FNN-P&O scheme was tested under PSCs. Starting from STCs, changes in solar irradiance were applied to the modules according to three test scenarios:

- Scenario 2: run under STCs for 0.5 s to achieve a steady state and then step G_2 down to 200 W/m² and G_3 down to 400 W/m² at t = 0.5 s.
- Scenario 3: run under STCs for 0.5 s to achieve a steady state and then step G_2 down to 600 W/m² and G_3 down to 800 W/m² at t = 0.5 s.
- Scenario 4: continuously adjust G_1, G_2, and G_3 according to the profile shown in Figure 14.

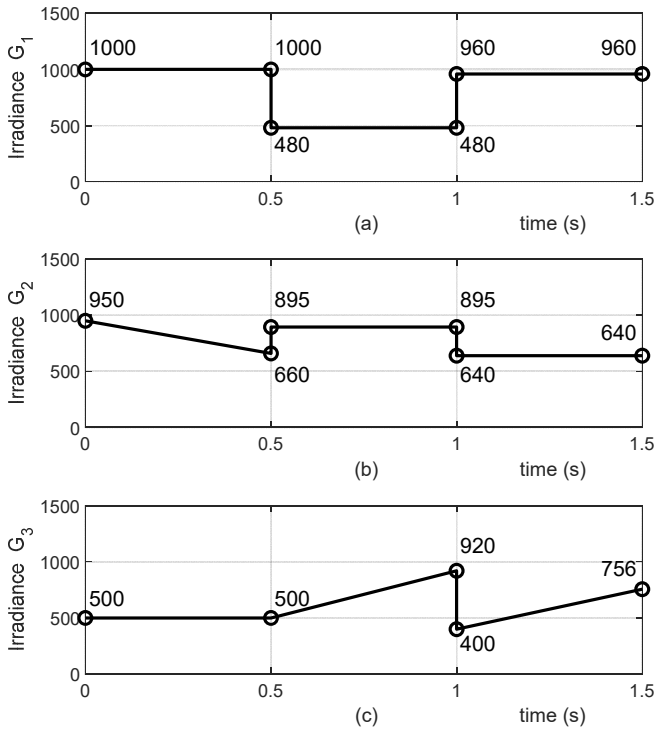

Figure 14. Irradiance variation profile for Scenario 4: (**a**) G_1, (**b**) G_2, and (**c**) G_3 over a 1.5 s interval.

Across the three scenarios, multiple power peaks emerge as a result of non-uniform irradiance across the panels. Scenario 2 exhibits approximate peak values of 187.6 W, 173.1 W, and 133.9 W on the *P-V* curve (see Figure 4b); Scenario 3 reaches values of 396.7 W, 187.5 W, and 331.6 W (see Figure 4d). Figures 15 and 16 depict the comparative responses of the three algorithms under rapid PSCs occurring at t = 0.5 s for Scenario 2.

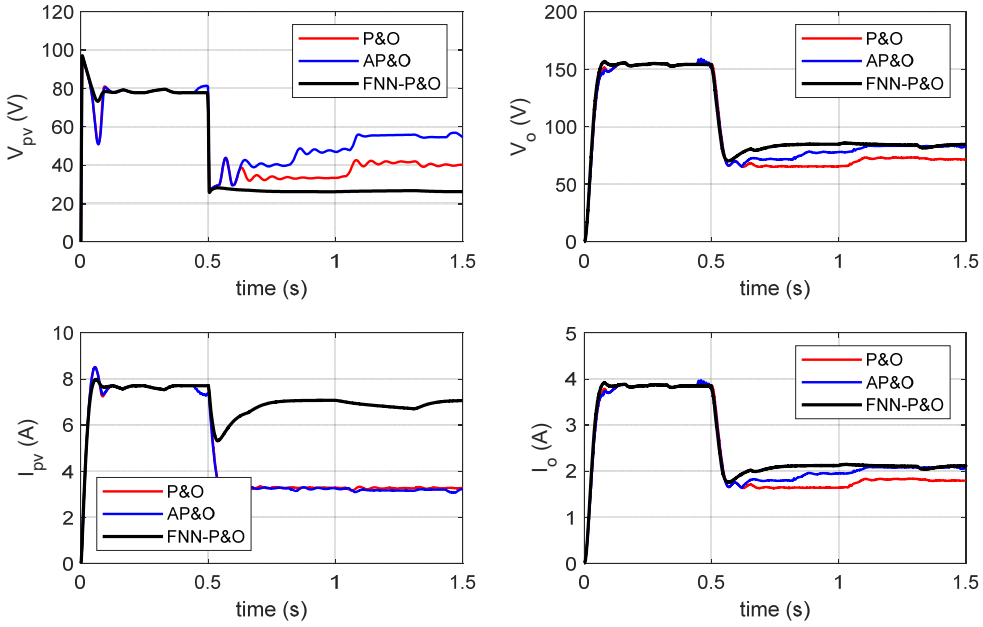

Figure 15. Dynamic response comparison of V_{pv}, I_{pv}, V_o and I_o for the P&O, AP&O, and FNN-P&O methods under Scenario 2.

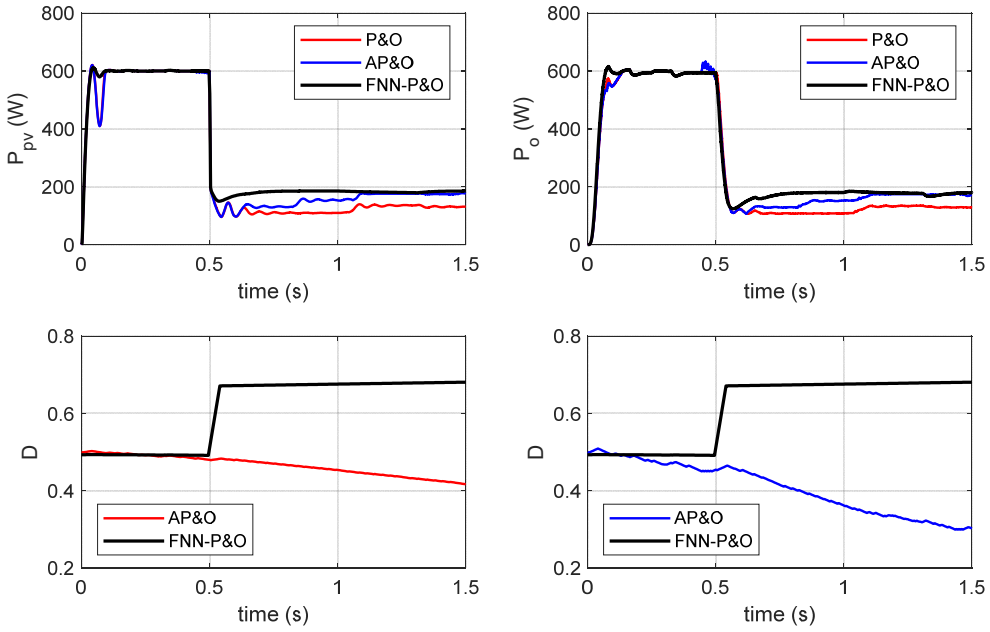

Figure 16. Dynamic response comparison of P_{pv}, P_o and D for the P&O, AP&O, and FNN-P&O methods under Scenario 2.

Table 3 details the corresponding quantitative performance metrics. Note that the overshoot of P_{pv} was evaluated during the transient interval from 0.5 to 1.5 s, while the remaining metrics were computed over the full time duration. As shown in Figure 16, FNN-P&O successfully tracks the GMPP at 187.6 W with M_p = 8.48%, while P&O gets trapped at a local peak of 173.1 W. Setting parameter α to 0.002 prevents AP&O from being trapped in local maxima and allows it to approach the GMPP, albeit at the expense of transient oscillations with M_p = 21.49%. Additionally, FNN-P&O attains the highest tracking efficiency at 97.25% with the lowest energy loss of 15.26 J, outperforming P&O and AP&O. FNN-P&O transitions smoothly to the updated D_{mpp} (0.714) at 0.5 s.

Table 3. Quantitative performance metrics of the three methods under Scenario 2.

Method	Performance Metric		
	M_p (%)	η_{mpp} (%)	E_{loss} (J)
P&O	21.50	84.41	77.67
AP&O	21.49	90.96	45.99
FNN-P&O	8.48	97.25	15.26

Figures 17 and 18 illustrate the simulation results for Scenario 3, and the corresponding performance metrics evaluated over time ($0.5 < t \leq 1$ s) are summarized in Table 4.

Table 4. Quantitative performance metrics of the three methods under Scenario 3.

Method	Performance Metric		
	M_p (%)	η_{mpp} (%)	E_{loss} (J)
P&O	80.57	88.23	83.20
AP&O	61.95	92.38	57.48
FNN-P&O	64.46	98.41	15.73

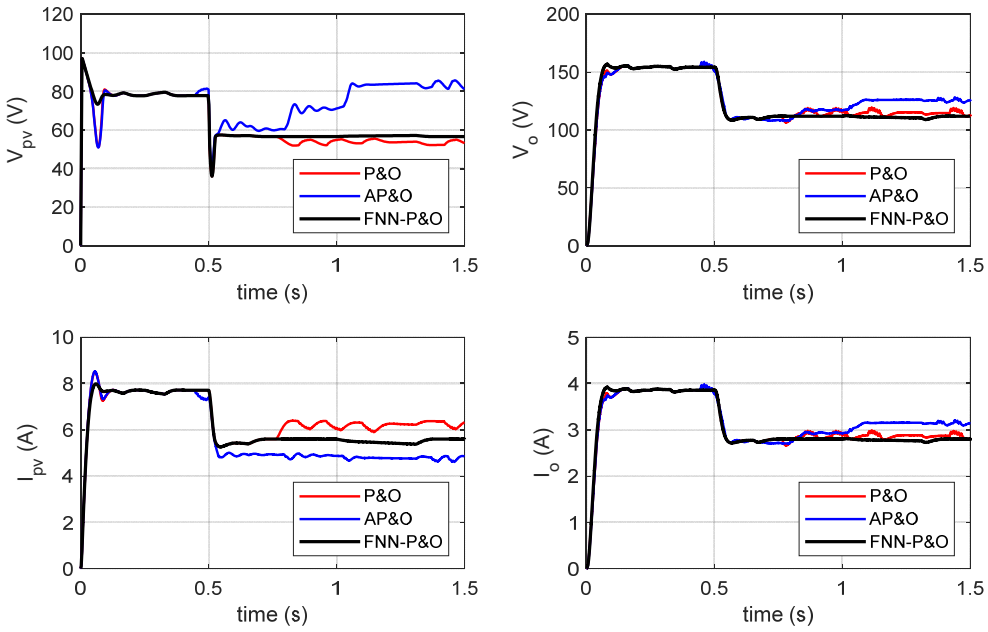

Figure 17. Dynamic response comparison of V_{pv}, I_{pv}, V_o and I_o for the P&O, AP&O, and FNN-P&O methods under Scenario 3.

Following the transition at t = 0.5 s, FNN-P&O's P_{pv} rapidly converges to the GMPP of 396.7 W with minimal delay. AP&O eventually tracks the GMPP near t = 1.05 s, but suffers from transient oscillations, yielding M_p = 61.95%. In contrast, P&O fails to reach the true peak and remains trapped at a local power level of 331.6 W, incurring a severe overshoot of 80.57%. Overall, FNN-P&O achieves superior steady-state tracking efficiency (98.41%) and drastically reduces total energy loss to 15.73 J, representing a 72.6% reduction relative to AP&O (57.48 J) and an 81.1% reduction compared to P&O (83.20 J). The relatively large M_p of FNN-P&O (64.46%) reflects the transient power dip immediately after the abrupt irradiance drop; this dip is short-lived, after which FNN-P&O settles at the GMPP, whereas AP&O remains below the GMPP until approximately t = 1.05 s.

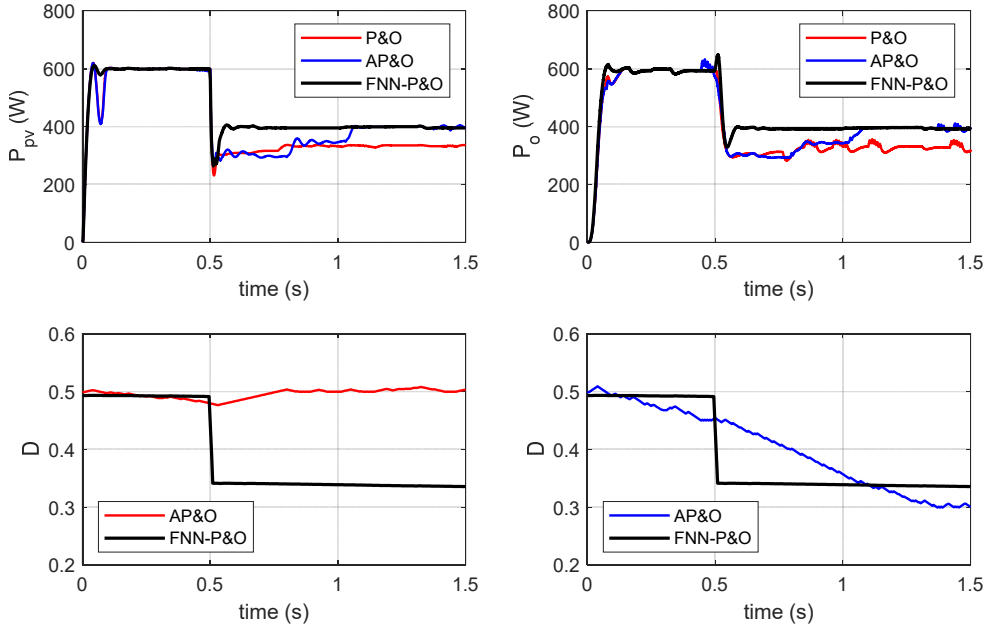

Figure 18. Dynamic response comparison of P_{pv}, P_o and D for the P&O, AP&O, and FNN-P&O methods under Scenario 3.

Figures 19 and 20 show the simulation results under continuous PSC changes starting from t = 0 s for Scenario 4. Table 5 summarizes two performance metrics.

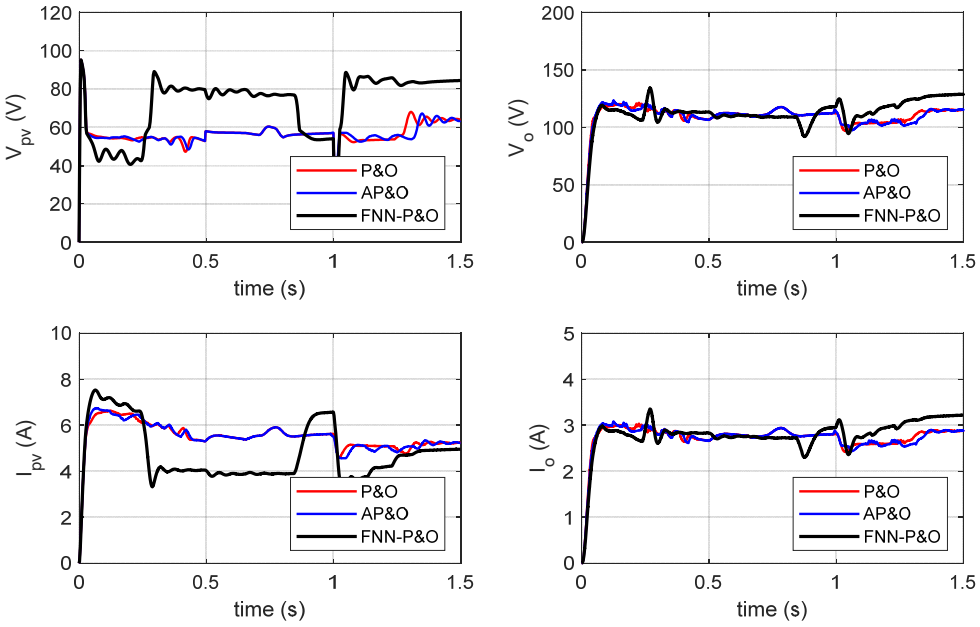

Figure 19. Dynamic response comparison of V_{pv}, I_{pv}, V_o and I_o for the P&O, AP&O, and FNN-P&O methods under Scenario 4.

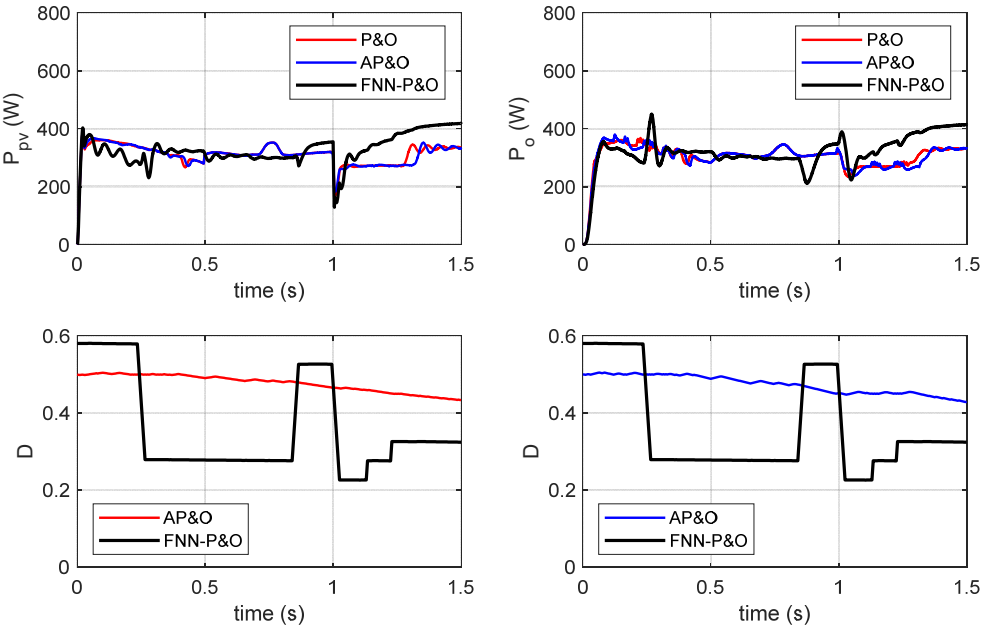

Figure 20. Dynamic response comparison of P_{pv}, P_o and D for the P&O, AP&O, and FNN-P&O methods under Scenario 4.

Table 5. Quantitative performance metrics of the three methods under Scenario 4.

Method	Performance Metric		
	M_p (%)	η_{mpp} (%)	E_{loss} (J)
P&O	-	90.50	53.79
AP&O	-	90.12	55.66
FNN-P&O	-	94.97	30.10

In Scenario 4, the FNN-P&O algorithm demonstrates superior performance compared to both P&O and AP&O under rapid dynamic conditions. By integrating a neural network, the PV system achieves swift and precise duty-cycle control, thereby minimizing transient energy losses and maximizing overall power conversion efficiency.

4.3.3. Scenario 5: Varying Cell Temperature

The final simulation evaluates the performance of the proposed algorithm under changing thermal conditions. The cell temperature T was stepped from 25 °C to 15 °C at 0.5 s. All three panels were initially set to STCs and subjected to identical temperature variations, assuming they share the same physical space. Figures 21 and 22 depict the transient responses for Scenario 5 using the three algorithms. Table 6 summarizes the performance metrics evaluated during $0.5 < t \leq 1$ s.

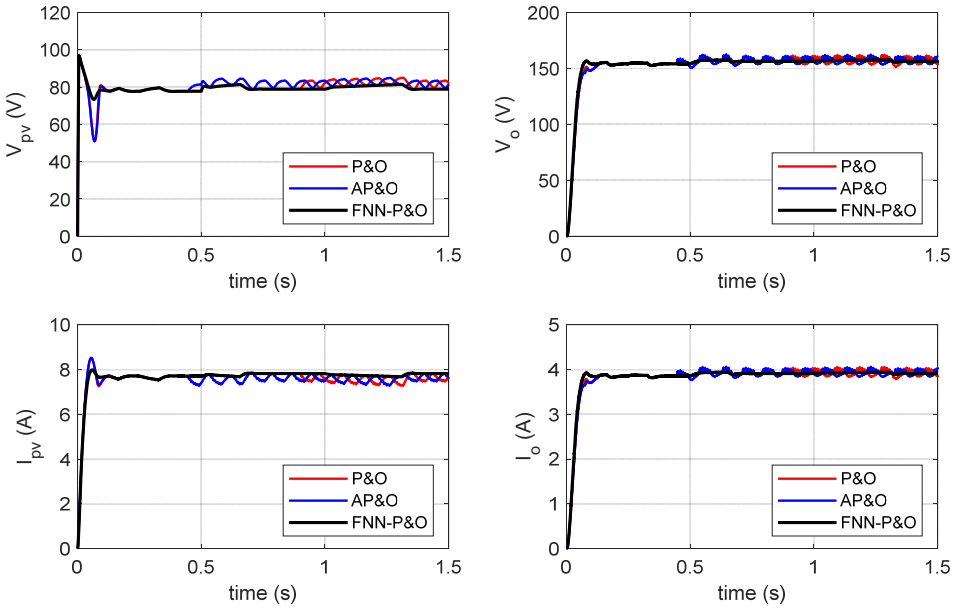

Figure 21. Dynamic response comparison of V_{pv}, I_{pv}, V_o and I_o for the P&O, AP&O, and FNN-P&O methods under varying cell temperature.

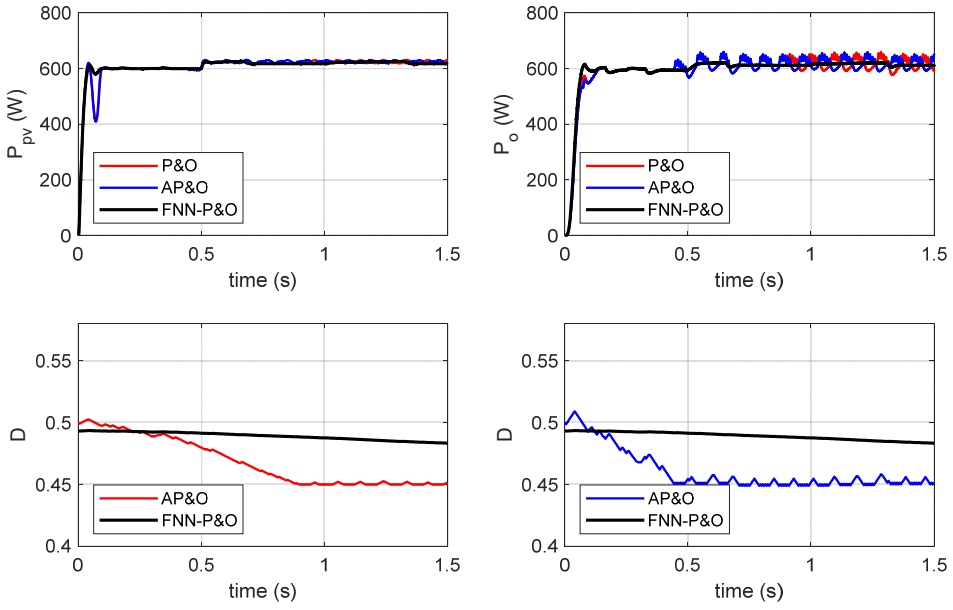

Figure 22. Dynamic response comparison of P_{pv}, P_o and D for the P&O, AP&O, and FNN-P&O methods under varying cell temperature.

All three algorithms transition to the new peak power level near 620 W during the step change. However, P&O and AP&O display a poorer transient response than FNN-P&O. The percentage overshoots for P&O and AP&O were omitted because both algorithms exhibited continuous oscillations. As detailed in quantitative metrics in Table 6, the proposed FNN-P&O algorithm achieves the highest tracking efficiency (99.31%) while resulting in the lowest absolute energy loss (13.16 J). In comparison, P&O and AP&O yield slightly lower tracking efficiencies of 99.09% and 99.26%, respectively, while generating noticeably higher energy losses of 19.55 J and 21.88 J.

Table 6. Quantitative performance metrics of the three methods under Scenario 5.

Method	Performance Metric		
	M_p (%)	η_{mpp} (%)	E_{loss} (J)
P&O	-	99.09	19.55
AP&O	-	99.26	21.88
FNN-P&O	21.75	99.31	13.16

5. Conclusions

This study successfully developed and evaluated a hybrid FNN-P&O MPPT control architecture for a PV-fed DC-DC boost converter operating under PSCs. By integrating FNN-based D_{mpp} prediction with small-step perturbation, the proposed method effectively resolves the key drawbacks of traditional gradient-based MPPT algorithms. The primary findings of this research are summarized as follows:

- The HGA successfully identified the single-diode equivalent parameters for the Kyocera KC200GT PV cell, achieving an R^2 fitting accuracy of 99.96% against the datasheet data.
- By extending the derived cell model formulas into series and parallel configurations, the model readily scales to represent complex modules or strings for estimating D_{mpp} across changing environments.
- Under PSCs with multi-peak *P-V* curves, FNN-P&O consistently tracks the GMPP. In contrast, P&O becomes trapped at sub-optimal local peaks, while AP&O converges near the GMPP only at the expense of transient oscillations.
- The proposed method achieves rapid GMPP tracking with short-lived transients and suppressed steady-state oscillations, delivering higher tracking efficiency and lower energy loss than P&O and AP&O under both STCs and PSCs.

Follow-up work will focus on hardware implementation and experimental testing of the proposed method and designing a dual-stage power conversion system that combines MPPT control and voltage regulation.

Author Contributions: Conceptualization, formal analysis, methodology, software, visualization, writing—original draft preparation, G.G.J.; data curation, resources, writing—review and editing, U.O., O.Y., Y.L.; investigation, writing—review and editing, supervision, funding acquisition, J.L. All authors have read and agreed to the published version of the manuscript.

Funding: This study was funded by the Korea Institute of Ocean Science and Technology (KIOST) research program (PEB0021).

Institutional Review Board Statement: Not applicable.

Informed Consent Statement: Not applicable.

Data Availability Statement: The datasets used and/or analyzed during the current study are available from the corresponding author upon reasonable request.

Conflicts of Interest: The authors declare no conflicts of interest.

References

1. Motahhir, S.; Eltamaly, A.M. (Eds.) *Advanced Technologies for Solar Photovoltaics Energy Systems*; Springer Nature: Cham, Switzerland, 2021. https://doi.org/10.1007/978-3-030-64565-6.
2. Duffie, J.A.; Beckman, W.A.; Blair, N. *Solar Engineering of Thermal Processes, Photovoltaics and Wind*, 5th ed.; John Wiley & Sons: Hoboken, NJ, USA, 2020. https://doi.org/10.1002/9781119540328.
3. Tong, N.T.; Pora, W. A parameter extraction technique exploiting intrinsic properties of solar cells. *Appl. Energy* **2016**, *176*, 104–115. https://doi.org/10.1016/j.apenergy.2016.05.064.
4. Derick, M.; Rani, C.; Rajesh, M.; Farrag, M.E.; Wang, Y.; Busawon, K. An improved optimization technique for estimation of solar photovoltaic parameters. *Sol. Energy* **2017**, *157*, 116–124. https://doi.org/10.1016/j.solener.2017.08.006.
5. Jervase, J.A.; Bourdoucen, H.; Al-Lawati, A. Solar cell parameter extraction using genetic algorithms. *Meas. Sci. Technol.* **2001**, *12*, 1922–1925. https://doi.org/10.1088/0957-0233/12/11/322.
6. Sharma, A.; Sharma, A.; Averbukh, M.; Jately, V.; Azzopardi, B. An Effective Method for Parameter Estimation of a Solar Cell. *Electronics* **2021**, *10*, 312. https://doi.org/10.3390/electronics10030312.
7. Herbazi, R.; Amechnoue, K.; Chahboun, A. Enhancement of Electrical Parameter Extraction from Solar Cells Using a Hybrid Genetic Algorithm with the Levenberg-Marquardt Method. *E3S Web Conf.* **2025**, *601*, 00053. https://doi.org/10.1051/e3sconf/202560100053.
8. Hussein, K.H.; Muta, I.; Hoshino, T.; Osakada, M. Maximum photovoltaic power tracking: An algorithm for rapidly changing atmospheric conditions. *IEE Proc.-Gener. Transm. Distrib.* **1995**, *142*, 59–64. https://doi.org/10.1049/ip-gtd:19951577.
9. Hohm, D.P.; Ropp, M.E. Comparative study of maximum power point tracking algorithms using an experimental, programmable, maximum power point tracking test bed. In Proceedings of the 28th IEEE Photovoltaic Specialists Conference, Anchorage, AK, USA, 15–22 September 2000; pp. 1699–1702. https://doi.org/10.1109/PVSC.2000.916230.
10. Femia, N.; Petrone, G.; Spagnuolo, G.; Vitelli, M. Optimization of perturb and observe maximum power point tracking method. *IEEE Trans. Power Electron.* **2005**, *20*, 963–973. https://doi.org/10.1109/TPEL.2005.850975.
11. Li, J.; Lu, S.; Yang, J. Multi-Stage Cooperative Optimization Control for Photovoltaic MPPT: A High-Efficiency Gray Wolf Optimizer–Incremental Conductance Hybrid Strategy. *Energies* **2025**, *18*, 1977. https://doi.org/10.3390/en18081977.
12. Fathurrahman, F.; Utami, R.S.; Akhyar, A.; Saddami, K. Adaptive P&O algorithm for fast and acurate maximum power point tracking for PV system. *Int. J. Appl. Power Eng.* **2026**, *15*, 590–599. https://doi.org/10.11591/ijape.v15.i2.pp590-599.
13. Almi, M.F.; Belmili, H.; Arrouf, M.; Bendib, B. A Novel Adaptive Variable Step Size P&O MPPT Algorithm. *Acad. J. Sci.* **2016**, *6*, 533–540.
14. Shaiek, Y.; Ben Smida, M.; Sakly, A.; Mimouni, M.F. Comparison between conventional methods and GA approach for maximum power point tracking of shaded solar PV generators. *Sol. Energy* **2013**, *90*, 107–122. https://doi.org/10.1016/j.solener.2013.01.005.
15. Daraban, S.; Petreus, D.; Morel, C. A novel MPPT algorithm based on a modified genetic algorithm specialized on tracking the global maximum power point in photovoltaic systems affected by partial shading. *Energy* **2014**, *74*, 374–388. https://doi.org/10.1016/j.energy.2014.07.001.
16. Hadji, S.; Gaubert, J.P.; Krim, F. Real-time genetic algorithms-based MPPT: Study and comparison (theoretical and experimental) with conventional methods. *Energies* **2018**, *11*, 459. https://doi.org/10.3390/en11020459.
17. Miyatake, M.; Veerachary, M.; Toriumi, F.; Fujii, N.; Ko, H. Maximum Power Point Tracking of Multiple Photovoltaic Arrays: A PSO Approach. *IEEE Trans. Aerosp. Electron. Syst.* **2011**, *47*, 367–380. https://doi.org/10.1109/TAES.2011.5705681.
18. Hayder, W.; Ogliari, E.; Dolara, A.; Abid, A.; Hamed, M.B.; Sbita, L. Improved PSO: A comparative study in MPPT algorithm for PV system control under partial shading conditions. *Energies* **2020**, *13*, 2035. https://doi.org/10.3390/en13082035.
19. Baatiah, A.O.; Eltamaly, A.M.; Alotaibi, M.A. Improving Photovoltaic MPPT Performance through PSO Dynamic Swarm Size Reduction. *Energies* **2023**, *16*, 6433. https://doi.org/10.3390/en16186433.
20. Premkumar, M.; Sowmya, R. An effective maximum power point tracker for partially shaded solar photovoltaic systems. *Energy Rep.* **2019**, *5*, 1445–1462. https://doi.org/10.1016/j.egyr.2019.10.006.
21. Wei, L.; Kou, Q. Research on MPPT Control Based on Novel Intelligent Fusion Algorithm in Photovoltaic-Storage DC Grid-Connected Systems. *Sustainability* **2026**, *18*, 2239. https://doi.org/10.3390/su18052239.
22. Nagadurga, T.; Raju, V.D.; Barnawi, A.B.; Bhutto, J.K.; Razak, A.; Wodajo, A.W. Global MPPT optimization for partially shaded photovoltaic systems. *Sci. Rep.* **2025**, *15*, 10831. https://doi.org/10.1038/s41598-025-89694-7.

23. Yap, K.Y.; Sarimuthu, C.R.; Lim, J.M.-Y. Artificial Intelligence Based MPPT Techniques for Solar Power System: A Review. *J. Mod. Power Syst. Clean Energy* **2020**, *8*, 1043–1059. https://doi.org/10.35833/MPCE.2020.000159.
24. Algarín, C.R.; Giraldo, J.T.; Álvarez, O.R. Fuzzy Logic Based MPPT Controller for a PV System. *Energies* **2017**, *10*, 2036. https://doi.org/10.3390/en10122036.
25. Laxman, B.; Annamraju, A.; Srikanth, N.V. A grey wolf optimized fuzzy logic based MPPT for shaded solar photovoltaic systems in microgrids. *Int. J. Hydrogen Energy* **2021**, *46*, 10653–10665. https://doi.org/10.1016/j.ijhydene.2020.12.158.
26. Abouzeid, A.F.; Eleraky, H.; Kalas, A.; Rizk, R.; Elsakka, M.M.; Refaat, A. Experimental validation of a low-cost maximum power point tracking technique based on artificial neural network for photovoltaic systems. *Sci. Rep.* **2024**, *14*, 18280. https://doi.org/10.1038/s41598-024-67306-0.
27. Dawahdeh, A.; Sharadga, H.; Kumar, S. Novel MPPT Controller Augmented with Neural Network for Use with Photovoltaic Systems Experiencing Rapid Solar Radiation Changes. *Sustainability* **2024**, *16*, 1021. https://doi.org/10.3390/su16031021.
28. Ali, M.N.; Mahmoud, K.; Lehtonen, M.; Darwish, M.M.F. Promising MPPT Methods Combining Metaheuristic, Fuzzy-Logic and ANN Techniques for Grid-Connected Photovoltaic. *Sensors* **2021**, *21*, 1244. https://doi.org/10.3390/s21041244.
29. Giraldo, L.F.; Gaviria, J.F.; Torres, M.I.; Alonso, C.; Bressan, M. Deep reinforcement learning using deep Q network for global maximum power point tracking: Design and experiments in real photovoltaic systems. *Heliyon* **2024**, *10*, e37974. https://doi.org/10.1016/j.heliyon.2024.e37974.
30. Wadehra, A.; Bhalla, S.; Jaiswal, V.; Rana, K.P.S.; Kumar, V. A deep recurrent reinforcement learning approach for enhanced MPPT in PV systems. *Appl. Soft Comput.* **2024**, *162*, 111728. https://doi.org/10.1016/j.asoc.2024.111728.
31. Yin, L.; Li, J.; Wang, N.; Gao, F. Deep predictive data representation model control for photovoltaic maximum power point tracking under partial shading conditions. *Energy Convers. Manag.* **2024**, *322*, 119171. https://doi.org/10.1016/j.enconman.2024.119171.
32. Messenger, R.A.; Abtahi, H.A. *Photovoltaic Systems Engineering*, 5th ed.; CRC Press: Boca Raton, FL, USA, 2024.
33. Kyocera Solar, Inc. *KC200GT High Efficiency Multicrystal Photovoltaic Module Datasheet*; Kyocera Solar, Inc.: Scottsdale, AZ, USA, 2014.
34. Khatib, T.; Elmenreich, W. *Modeling of Photovoltaic Systems Using MATLAB*; John Wiley & Sons: Hoboken, NJ, USA, 2016. https://doi.org/10.1002/9781119118138.
35. Jin, G.G.; Jarso, A.K. An improved hybrid genetic algorithm using the affine combination-based reproduction. *Commun. Stat. Simul. Comput.* **2025**, *54*, 3763–3789. https://doi.org/10.1080/03610918.2024.2363958.
36. Vieira, R.G.; de Araújo, F.M.U.; Dhimish, M.; Guerra, M.I.S. A Comprehensive Review on Bypass Diode Application on Photovoltaic Modules. *Energies* **2020**, *13*, 2472. https://doi.org/10.3390/en13102472.
37. MathWorks. *A Practical Guide to Deep Learning: From Data to Deployment*, 2nd ed.; The MathWorks, Inc.: Natick, MA, USA, 2021. Available online: https://www.mathworks.com/campaigns/pocket-guides/practical-guide-to-deep-learning.html (accessed on 16 October 2026).
38. Al-Malah, K. *Machine and Deep Learning Using MATLAB: Algorithms and Tools for Scientists and Engineers*; John Wiley & Sons: Hoboken, NJ, USA, 2024. https://doi.org/10.1002/9781394209118.

Disclaimer/Publisher's Note: The statements, opinions and data contained in all publications are solely those of the individual author(s) and contributor(s) and not of MDPI and/or the editor(s). MDPI and/or the editor(s) disclaim responsibility for any injury to people or property resulting from any ideas, methods, instructions or products referred to in the content.